54–67 Nucleic Acids Research, 2023, Vol. 51, No. 1 Published online 5 January 2023
https://doi.org/10.1093/nar/gkac1227

Structure-based investigations of the NAD+-II riboswitch

Xiaochen Xu[1,2,†], Michaela Egger[3,†], Chunyan Li[2,†], Hao Chen[2], Ronald Micura[3,*] and Aiming Ren[1,2,*]

[1]Department of Gastroenterology/Department of Cardiology of the Second Affiliated Hospital, School of Medicine, Zhejiang University, Hangzhou, Zhejiang 310058, China, [2]Life Sciences Institute, Zhejiang University, Hangzhou, Zhejiang 310058, China and [3]Institute of Organic Chemistry, Center for Molecular Biosciences Innsbruck, University of Innsbruck, Innsbruck 6020, Austria

Received October 12, 2022; Revised December 07, 2022; Editorial Decision December 07, 2022; Accepted December 10, 2022

ABSTRACT

Riboswitches are conserved non-coding domains in bacterial mRNA with gene regulation function that are essential for maintaining enzyme co-factor metabolism. Recently, the *pnuC* RNA motif was reported to selectively bind nicotinamide adenine dinucleotide (NAD+), defining a novel class of NAD+ riboswitches (NAD+-II) according to phylogenetic analysis. To reveal the three-dimensional architecture and the ligand-binding mode of this riboswitch, we solved the crystal structure of NAD+-II riboswitch in complex with NAD+. Strikingly and in contrast to class-I riboswitches that form a tight recognition pocket for the adenosine diphosphate (ADP) moiety of NAD+, the class-II riboswitches form a binding pocket for the nicotinamide mononucleotide (NMN) portion of NAD+ and display only unspecific interactions with the adenosine. We support this finding by an additional structure of the class-II RNA in complex with NMN alone. The structures define a novel RNA tertiary fold that was further confirmed by mutational analysis in combination with isothermal titration calorimetry (ITC), and 2-aminopurine-based fluorescence spectroscopic folding studies. Furthermore, we truncated the *pnuC* RNA motif to a short RNA helical scaffold with binding affinity comparable to the wild-type motif to allude to the potential of engineering the NAD+-II motif for biotechnological applications.

INTRODUCTION

Riboswitches are RNA gene regulatory elements that commonly reside in the 5′-end non-coding region of bacterial mRNA (1–4). They contain two domains, a small molecule-sensing aptamer domain and an adjoining expression platform. Binding of the cognate ligand to the aptamer induces a structural output of the expression platform that is distinct from the unbound form, and consequently, expression of the down-stream encoded protein is affected; it is boosted or diminished (5–9). In most cases, riboswitches regulate the genes that are involved in the ligand biosynthesis or transport (10–14). On a molecular basis, the most frequently encountered mechanism involves transcription or translation. Thereby, the interplay between the metabolite-sensing domain and the expression platform promotes formation of a terminator versus anti-terminator stem (transcription) or a repressor versus anti-repressor stem (translation).

More than 55 riboswitches have been identified to date, sensing structurally diverse small molecules with high selectivity (15,16). Many of these ligands are protein enzyme cofactors, such as *S*-adenosyl methionine (SAM), flavin adenine mononucleotide (FMN), tetrahydrofolate (THF), nicotinamide adenine dinucleotide (NAD^+) and many more (17). Riboswitches crucially participate in cofactor metabolism and regulate their intracellular concentrations, which is vital to maintain the cellular functions. For instance, NAD^+ possesses unique electron transport properties and works as a universal cellular electron transporter involved in many reduction-oxidation reactions. Structurally, NAD^+ is composed of two parts, nicotinamide riboside (NR) and adenosine, which are linked by a diphosphate group (Figure 1A). Though NAD^+ is one of the most abundant enzyme cofactors, the first NAD^+-sensing riboswitches had been identified only recently (18,19). This NAD^+-sensing riboswitch, later assigned to the NAD^+ class I riboswitch, relies on the *nadA* RNA motif identified in the phylum *Acidobateria* (18). It contains two tandemly arrayed aptamer domains with nearly identical folds. In earlier work, we solved the three-dimensional structures of both aptamer domains, revealed their significantly distinct affini-

*To whom correspondence should be addressed. Tel: +86 571 88981228; Fax: +86 571 88981227; Email: aimingren@zju.edu.cn
Correspondence may also be addressed to Ronald Micura. Email: ronald.micura@uibk.ac.at
†The authors wish it to be known that, in their opinion, the first three authors should be regarded as Joint First Authors.

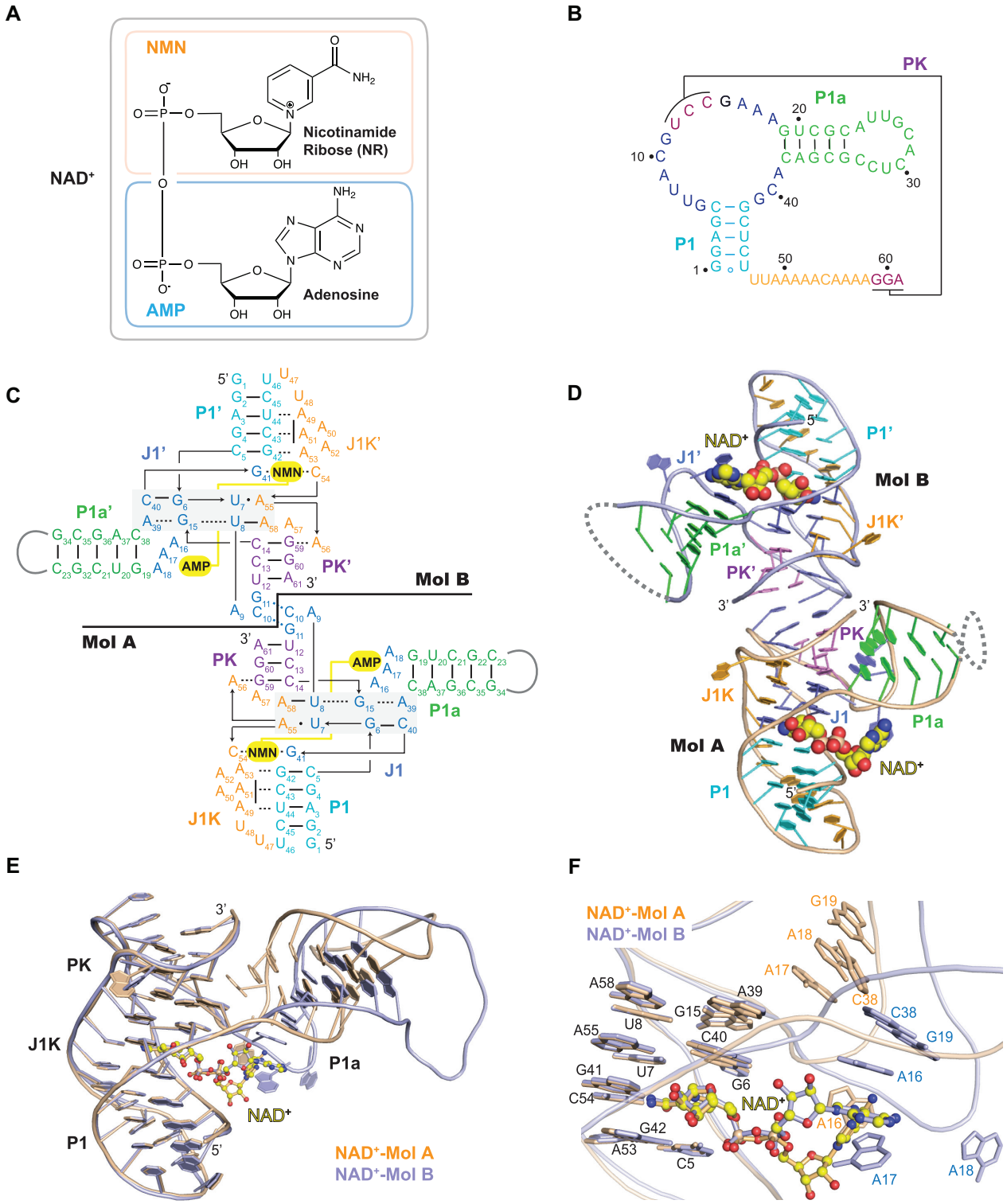

Figure 1. Secondary and tertiary structure of the dimeric NAD$^+$-II riboswitch in asymmetric unit. (**A**) Chemical structure of NAD$^+$ compound. NMN moiety and AMP moiety are highlighted with orange and light blue respectively. (**B**) Predicted second structure of the NAD$^+$-II riboswitch construct used in crystallization. (**C**) Schematic representation of the tertiary structure of dimeric NAD$^+$-II riboswitch in complex with NAD$^+$. Long distance interactions are labelled with dotted lines. Different modules are distinguished by varying colours. (**D**) Cartoon representation of the tertiary structure of dimeric NAD$^+$-II riboswitch in complex with NAD$^+$. The phosphate backbone of Mol A is shown in golden and the phosphate backbone of Mol B is shown in light blue. The base of two NAD$^+$-II riboswitch molecules are colour-coded as in (**B**). The ligands NAD$^+$ are shown in spheres. (**E**) Alignment of the two NAD$^+$-II riboswitch molecules structures. Mol A is shown in golden and Mol B is shown in light blue. (**F**) Alignment of the ligand binding pocket of the two NAD$^+$-II riboswitch molecules structures. The ligands NAD$^+$ are shown in stick and sphere.

ties to the ligand, and finally proposed a two-concentration sensor model for gene regulation by this riboswitch (20). Importantly, the NAD^+-I aptamer specifically recognizes the ADP moiety of NAD^+ (18,20,21).

Recently, a second class of NAD^+-sensing riboswitches (NAD^+-II) was identified based on the *pnuC* RNA motif in species of *Streptococcus* using comparative sequence analysis (22). The consensus sequence and secondary structure model of the *pnuC* RNA motif is shown in Supplementary Figure S1A, which consists of two stems (P1 and P1a) connected by an internal bubble. One possible pseudoknot stem (PK) was predicted to be formed between the internal bubble and a putative ribosome binding site (RBS) sequence located at the 3′-end, which suggested that the *pnuC* RNA motif may serve as a translationally controlled, genetic off-switch (22). In-line probing experiments indicated that the *pnuC* RNA motif recognizes the NMN-containing moiety of NAD^+ (22).

To reveal the three-dimensional architecture of the NAD^+-II riboswitch and to shed light on the NAD^+ ligand-binding mode, we set out for crystallographic studies. Here, we report the crystal structures of the *pnuC* RNA motif in complex with NAD^+ at the resolution of 2.2 Å, complemented by a second structure of the NAD^+-II RNA in complex with NMN at the resolution of 2.5 Å. In short, these structures reveal a novel RNA tertiary fold with a rigid binding pocket specific for NMN. The structures are verified by structure-guided mutational analysis in combination with ligand binding assays using isothermal titration calorimetry (ITC). Moreover, we shed light on the ligand-induced folding process of the aptamer domain by 2-aminopurine (Ap)-based fluorescence spectroscopy. Based on the information obtained from the tertiary structure and structural dynamics, we further tailor the NAD^+-II RNA by deletion one of the stems and demonstrate that the truncated version of the NAD^+-II RNA retains ligand binding affinity that is comparable to the wildtype RNA. Taken together, our study delivers a profound structural basis for the NAD^+-II riboswitch and illustrates the principles underlying its unique recognition pattern and folding path. Moreover, our work also provides a representative example for the tailoring and simplification of a native RNA motif which may lay the foundation for engineering of a cofactor sensor as biotechnological tool.

MATERIALS AND METHODS

RNA preparation

In order to promote the crystallization of NAD^+-II riboswitch-NAD^+ complex, we introduced UNCG, GNRA or U1A protein-binding loop into the position of variable loop of the P1a stem. The *pnuC* RNA sequence followed by the HDV ribozyme was inserted into pUT7 plasmid containing T7 promoter, which was amplified by polymerase chain reaction (PCR) to generate the DNA template for in vitro transcription (23). The in vitro transcription was performed with T7 RNA polymerase at 37°C for 4.5 h, followed by purification with urea–denatured polyacrylamide gel electrophoresis (urea–PAGE). RNA bands were visualized under the UV lamp, and the target RNA was excised and soaked in the 0.5× Tris–acetate–EDTA (TAE) buffer. The eluted RNA was precipitated with isopropanol, washed with 80% ethanol and further lyophilized. Finally, the lyophilized RNA was dissolved into diethyl pyrocarbonate (DEPC)-treated double-distilled water.

Ligands

NAD^+ was purchased from Yuanye Bio-Technology Co. Ltd (Shanghai). NMN was purchased from Sigma.

Crystallization

A final concentration of 0.4 mM RNA sample was annealed in the buffer containing 50 mM HEPES pH 7.0 (25°C), 50 mM NaCl and 5 mM $MgCl_2$ at 65°C for 5 min, cooled on ice for at least 30 min, and incubated with NAD^+ or NMN at a final concentration of 6 mM on ice for one additional hour. For the constructs containing U1A protein-binding loop, U1A protein was added to RNA at a ratio of 1.2:1 (U1A protein to RNA) and incubated for one more hour. Then the complex was mixed with the reservoir solution at a 1:1 ratio using sitting drop vapour diffusion method with the ARI Grphon-LCP-Nano robot at 16°C for crystallization screening. The high-resolution crystals of RNA-NAD^+ complex and RNA-NMN complex grew from the condition containing 0.2 M KCl, 0.01 M $MgCl_2$, 0.05 M MES pH 5.6 (25°C) and 5–10% PEG8000 in around one week. The crystals were transferred to the well solution with additional 30% glycerol and then flash-frozen in liquid nitrogen. The X-ray crystallography diffraction data was collected at the beamline BL19U1 at the Shanghai Synchrotron Radiation Facility (SSRF).

Structure determination and refinement

The diffraction data were processed using HKL3000 (HKL Research). The phase problem of NAD^+-II riboswitch-NAD^+ complex was solved by the Molecular Replacement program of CCP4 suite with the U1A protein structure as the initial model. The structure model was further built and refined in the Coot program and Phenix program (24–26). The structure of the NAD^+-II riboswitch-NMN complex was solved by the molecular replacement method with the NAD^+-II riboswitch-NAD^+ structure as the initial model, and further refined by the joint use of Coot and Phenix programs. The ligands were added into the structure at the last several runs of building and refinement based on their electron density map including $2F_o - F_c$ and $F_o - F_c$ maps and geometry. The statistics of X-ray diffraction data and structure refinement are shown in the Supplementary Table S1.

Isothermal titration calorimetry

All ITC experiments were performed on a MicroCal PEAQ-ITC calorimeter at 25°C at the National Center for Protein Science·Shanghai (NCPSS). Before the titration, the wild-type RNA carrying GAAA loop and mutant RNA samples were dialyzed overnight at 4°C in ITC buffer (50 mM

MOPS pH 7.5 (25°C), 100 mM KCl, 20 mM $MgCl_2$). To determine the effect of $MgCl_2$ on ligand recognition, the wild-type RNA carrying GAAA loop was dialyzed in ITC buffer supplemented with different concentrations of $MgCl_2$ varying from 0 mM to 20 mM. Then a final concentration of 0.15 mM RNA was annealed at 65°C for 5 min, cooled on ice for half an hour. Due to the lower heat changes of NAD^+ binding in some titrations, NMN was used to instead of NAD^+ in most titration experiments. NMN ligand was dissolved with each corresponding ITC buffer and diluted to 2 mM before use. The NMN ligand was titrated into RNA by initial injection of 0.4 μl, followed by 18 serial injections of 2 μl with 120 s intervals between injections and a reference power of 5 μcal s^{-1}. The titration data were analyzed by MicroCal PEAQ-ITC Analysis Software. All the thermodynamic binding parameters are shown in Supplementary Table S2.

Fluorescence spectroscopy

All steady-state fluorescence spectroscopic experiments were measured on a Cary Eclipse spectrometer (Varian, Australia) equipped with a peltier block, a magnetic stirring device and a RX2000 stopped-flow apparatus (Applied Photophysics Ltd, UK). The data obtained were processed with OriginPro 2018 software (OriginLab, USA). Aminopurine-modified RNA samples were prepared in 0.5 μM concentration in a total volume of 120 μl (qualitative analysis) or 1 ml (quantitative analysis) of buffer (50 mM MOPS, 100 mM KCl, pH 7.5 (25°C)). The samples were heated to 90°C for 2 min, allowed to cool to room temperature, transferred to quartz cuvettes equipped with a small stir bar and held at 20°C in the Peltier controlled sample holder. Then, ligands were manually pipetted in a way not to exceed a total volume increase of 3%. For binding affinity experiments, the solution was stirred after ligand addition and allowed to equilibrate for at least 15 min before data collection. Spectra were recorded from 320 to 500 nm using the following instrumental parameters: excitation wavelength, 308 nm; increments, 1 nm; scan rate, 120 nm min^{-1}; slit widths, 10 nm. Thermodynamic and kinetic parameters K_d and k_{obs} were obtained as described in reference (20).

RESULTS AND DISCUSSION

Design of NAD^+-II riboswitch constructs for crystallization

The *pnuC* motif constitutes the NAD^+-II riboswitch and is associated to proteins that are known to transport nicotinamide riboside (NR), a component of the cofactor NAD^+(22). The consensus secondary structure model derived from comparative sequence analysis suggests that the *pnuC* motif forms two stems (P1 and P1a) which are connected by a large internal loop (Supplementary Figure S1A) (22). A possible pseudoknot (PK) may fold between the internal loop (J1) and the long 3′-end tail (J1K). Most nucleotides in the *pnuC* motif are highly conserved except the variable terminal loop of stem P1a. Through *in vitro* transcription, we prepared a large number of NAD^+-II riboswitch constructs from various bacterial representatives for crystallization trials in the presence of NAD^+ or NMN (Figure 1A, B). One sequence from *Streptococcus* sp. with the variable loop of stem P1a replaced by the U1A recognition sequence, was co-crystallized with U1A protein and gave well-diffracting crystals (Figure 1B–D, Supplementary Figure S1B). The crystal structure of NAD^+-II riboswitch in complex with NAD^+ was determined at a resolution of 2.2 Å by molecular replacement with U1A protein as the initial model. Besides, we also solved the structure of NAD^+-II riboswitch in complex with NMN by molecular replacement at a resolution of 2.5 Å. The X-ray crystallographic statistics of the two structures are listed in Supplementary Table S1.

To determine the ligand binding affinity of NAD^+-II riboswitch, we used isothermal titration calorimetry (ITC). The dissociation constant K_d of the original RNA comprising the sequence AUUCCC as variable loop (*pnuC*-ori) and NMN was 58.6 ± 5.4 μM, with estimated thermodynamics parameters ΔH of –8.7 ± 0.3 kcal/mol and ΔS of –0.01 kcal/mol/K (Figure 1C, Supplementary Figure S2A and Supplementary Table S2). We also determined the binding affinity of one NAD^+-II riboswitch construct with a GAAA loop as variable loop (*pnuC*-GA) and NMN; this dissociation constant K_d amounted to 41.1 ± 1.1 μM, with estimated thermodynamics parameters ΔH of –11.7 ± 0.1 kcal/mol and ΔS of –0.019 kcal/mol/K, which is slightly lower compared to *pnuC*-ori (Figure 1C, Supplementary Figure S2 and Supplementary Table S2). The stoichiometry of binding approached 1:1 for both constructs.

Overall tertiary fold of the NAD^+ bound NAD^+-II riboswitch

The schematic secondary structure and the solved three-dimensional structure of the NAD^+ bound NAD^+-II riboswitch are illustrated in Figure 1C and D. In the crystal, each asymmetric unit contains two RNA molecules (Mol A and Mol B) that form a dimer through two consecutive base pairs C10(Mol A)-G11(Mol B) and C10(Mol B)-G11(Mol A), following each pseudoknot stem (PK and PK'). This arrangement results in a continuously stacked helix at the interface of the dimer (Supplementary Figure S3). We note that G11 in Mol A and Mol B both adopt a 2′-*endo* ribose conformation (Supplementary Figure S3A).

The overlay of Mol A and Mol B reveals very good alignment of stem P1, pseudoknot PK, and the segment J1K between stem P1 and PK (Figure 1E), while a twisted shift and distinct orientation is adopted by stem P1a and the linking segment between stem P1a and the large internal loop J1 (Figure 1E, F). The bound ligand NAD^+ in Mol A and Mol B are both located in the intersection of stems P1, P1a, internal loop J1 and tail J1K and have an open, spread-out conformation (Figure 1C–E). Detailed comparison of the bound ligand NAD^+ in Mol A (shown in gold) and Mol B (shown in light blue) shows that the NMN-moiety of the ligand NAD^+ adopts the same conformation and is wedged by the well-aligned stem P1, PK and J1K in similar way, while the ADP-moiety of NAD^+ shows flexibility and adopts distinct conformation to interact with the shifted linking segment including nucleotides A16, A17 and A18 (Figure 1E, F). As shown in Supplementary Figure S4A, A17 and A18 in Mol A form a successive stacking interaction on G19-C38, the inner first base pair of stem P1a, while A16 in Mol A stretches into the inner side of the intersection near the

ADP moiety of the bound NAD^+. In Mol B, A16 and A17 sandwich the adenine moiety of NAD^+ and stack on G19-C38, while A18 stretches out and forms no interaction with the rest of the RNA (Supplementary Figure S4B). The conformational flexibility of this part of the RNA (the linking segment G15-to-A18 between P1a and PK) is also reflected in the diversity of their sugar puckers. A16 in Mol A and Mol B both adopt the generally less populated *2′-endo* conformation. However, A17 and A18 adopt *3′-endo* conformation in Mol A, while they adopt *2′-endo* conformation in Mol B (Supplementary Figure S4).

Structural organization of the NAD^+-II riboswitch

The tertiary fold of the *pnuC* RNA–NAD^+ complex shown for Mol A in cartoon representation in Figure 2A and schematically in Figure 2B conforms with the predicted secondary structure model of the consensus sequence (Supplementary Figure S1A) (22). The major elements of the NAD^+-II riboswitch fold are two stems, P1 (in cyan) and P1a (in green), and one short pseudoknot stem PK (in violet) that together adopt a 'Y-shape' architecture (Figure 2A).

Stem P1 and PK exhibit co-axial stacking alignment mediated by the junctional regions J1 (in blue) and J1K (in orange), and the bound NAD^+; they thereby form a vertical compact helical scaffold (Figure 2A, B). Stem P1a is connected to the vertical helical scaffold by the linking nucleotides in J1 (G15 to A18 and A39 to G41) (Figure 2A, B). NAD^+ is bound at the intersection of stem P1, junction J1 and stem P1a, where the NR (nicotinamide riboside) moiety is deeply buried into a cavity upon stem P1, the diphosphate moiety is located along the major groove side of stem P1, and the adenosine moiety points outwards and stacks with nucleotides from J1.

As shown in Figure 2C-K, the nucleotides in the junction region of the NAD^+-II riboswitch form extensive tertiary interactions to define the overall folding and the NAD^+ binding pocket. In junction J1, the segment from G6 to A18 that connects stem P1 with P1a zippers up and interacts with the 3′-end terminal tail of J1K, which constitute the north terminal multi-tiered architecture of the NAD^+-II riboswitch above the bound NAD^+ (Figure 2C, Supplementary Figure S3C). As we mentioned before, C10 and G11 in J1 make up the dimer of the NAD^+-II riboswitch (Figure 1C, D and Supplementary Figure S3A-B). The following U12, C13 and C14 in J1 form the pseudoknot interaction (PK) with the last three nucleotides G59, G60 and A61 of J1K (Figure 2B, C). In the major groove side of stem PK, A9 from J1 interacts with the Hoogsteen edge of G60 through its Watson-Crick edge, forming the base triple C13-G60-A9 as the first tier (Figure 2D). Likewise, G59 not only forms a Watson-Crick base pair with C14 in stem PK, but also forms one hydrogen bond with the 6-NH2 of A56 from J1K through its O6, which constitutes the base triple C14-G59-A56 as the second tier (Figure 2E).

In junction J1K, four successive adenosines A55, A56, A57 and A58 are located before the terminal three nucleotides that form the pseudoknot stem PK (Figure 1B). While A57 points out of the helical structure without forming any interaction with other adjacent nucleotides, A55 and A56 sandwich A58 and form a continuous base staple (Figure 2C). In a tertiary long-range interaction, A58 forms a reverse Watson-Crick base pair with U8. Besides, the 2′-OH of A58 forms two additional hydrogen bonds with the sugar edge of A39. The base of A39 forms three hydrogen bonds with the sugar edge of G15 and the Watson-Crick edge of G15 interacts with the O4 of U8. Together this base tetrad U8-A58-A39-G15 (Figure 2F, Supplementary Figure S3C) represents the third tier that stacks upon the two base triple tiers, C14-G59-A56 and C13-G60-A9. Below the U8-A58-A39-G15 tier, two consecutive nucleotides G6 and U7 are positioned in one plane, where G6 forms a canonical Watson-Crick base pair with C40 and U7 forms a Hoogsteen base pair with A55. Besides the base pairing, the phosphate oxygen of A55 also forms two other hydrogen bonds with the sugar edge of U7. In addition, three hydrogen bonds are formed between G6-C40 and A55-U7. This base tetrad of G6-U7-C40-A55 represents the fourth and final tier, stacking upon the bound NAD^+ (Figure 2G, Supplementary Figure S3C).

Below the NAD^+ binding site, the nucleotides of J1K reside in the minor groove of stem P1 and form continuous stacking interactions (Figure 2H). Thereby, the five consecutive adenosines A49, A50, A51, A52 and A53 form comprehensive A-minor interaction with the top three base pairs of stem P1, generating a triple helical scaffold in the south part of the overall structure (Figure 2H). A53 forms three hydrogen bonds with the minor groove side of C5-G42, the north terminal base pair of stem P1 (Figure 2I). The following three nucleotide A52, A51 and A50 form hydrogen-bonding interaction with the minor groove side of G4-C43 in different ways (Figure 2J). A52 interacts with the G4-C43 base pair by forming one hydrogen bond with 2-NH2 of G4 and one hydrogen bond with O2 of C43 respectively. A51 forms two hydrogen bonds with the sugar edge of G4 on positions 2-NH2 and 2′-OH using its Watson-crick edge. A50 also forms two hydrogen bonds with the sugar edge of G4 on positions N3 and 2′-OH using its Hoogsteen edge (Figure 2J). Besides, 6-NH2 of A50 forms a hydrogen bond with O2 of U44 (Figure 2K), and A49 forms two hydrogen bonds with the ribose and N3 of A3 (Figure 2K). The following last two nucleotides U47 and U48 in J1K only form week interactions with the neighbour residues, and take a sharp 'U-turn' to connect with stem P1 at the south terminal of the NAD^+-II riboswitch (Figure 2H).

Binding pocket interactions of the NAD^+-II riboswitch with NAD^+

The binding pocket of the NAD^+-II riboswitch is located at the intersection of stem P1, P1a and PK, which are connected by the tightly packed junctional regions J1 and J1K (Figure 2A, B). In Figure 3A, the secondary structure scheme highlights the nucleotides of J1 and J1K that constitute the binding pocket. The surface representation of the NAD^+-II riboswitch NAD^+-binding pocket in the two asymmetric molecules are depicted in Figure 3B and C respectively; their comparison makes clear that the NMN moiety of NAD^+ intercalates between stem P1 and junction J1 and is intensively stacked in both two molecules. In con-

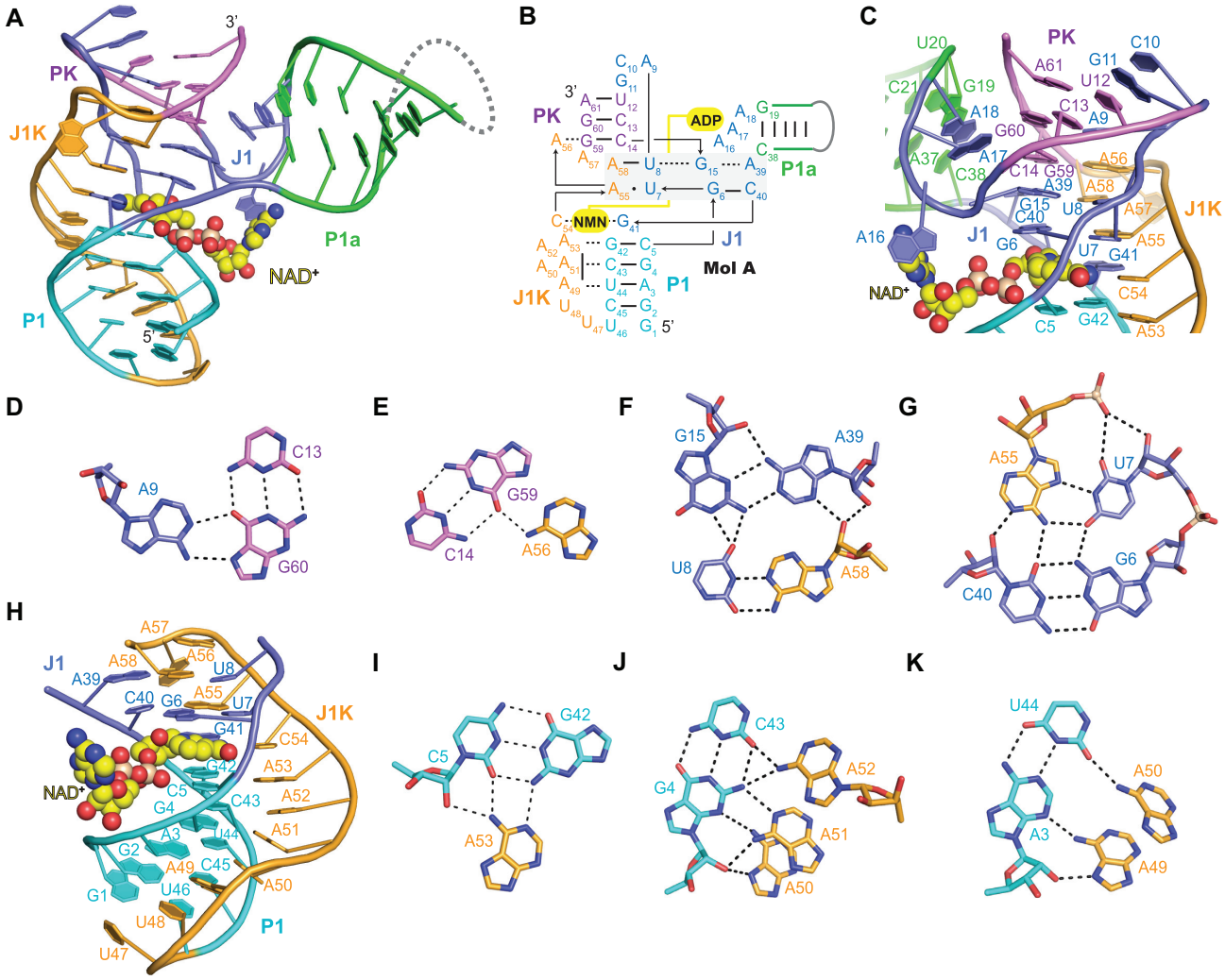

Figure 2. Secondary and tertiary structure of the NAD$^+$-II riboswitch bound to NAD$^+$. (**A**) Cartoon representation of the tertiary structure of NAD$^+$-II riboswitch in complex with NAD$^+$. Same colour code as in Figure 1 is used. (**B**) Schematic representation of the tertiary structure of NAD$^+$-II riboswitch. The non-conserved stem P1a and its variable loop are labelled with solid lines. (**C**) Structural organization of junction J1 and close-up view of the interactions between stem PK and junction J1. (**D**) C13 (PK) and G60 (PK) form Watson-Crick base pair, while the hoogsteen edge of G60 (PK) paired with the Watson-Crick edge of A9 (J1). (**E**) Base triple formed by C14 (PK), G59 (PK) and A56 (J1K). G59 (PK) Watson–Crick paired with C14 (PK) and its minor-groove recognizing the 6-NH2 of A56 (J1K). (**F**) Close-up view of the base quadruple U8-G15-A39-A58. (**G**) Close-up view of the base quadruple G6-U7-C40-A55 that forms the ceiling of the binding pocket. (**H**) Structural organization of 3′ terminal tail J1K and detailed interactions between stem P1 and 3′ terminal tail J1K. (**I**) Close-up view of the base triple C5-G42-A53 that forms the platform below the ligand. (**J**) A50, A51 and A52 from J1K hydrogen bond with the minor groove of the 2nd north terminal base pair G4-C43 from stem P1. (**K**) A49 and A50 from J1K hydrogen bond with the minor groove of the third north terminal base pair A3-U44 from stem P1.

trast, the AMP moiety of NAD$^+$ is in different orientation as is the evagination of J1.

Both binding pockets (Mol A and Mol B) are constituted by the base tetrad G6-U7-C40-A55 above the bound NAD$^+$ (Figure 2G, 3D), the base triple C5-G42-A53 below the bound NAD$^+$ (Figures 2I, 3D) and two nucleotides G41 in J1 and C54 in J1K (Figure 3D). C54 and G41 form a sheared base pair when interacting with the NMN moiety of NAD$^+$; importantly, the amide group of NMN forms three hydrogen bonds with the Watson-Crick edge of C54 and O6 of G41 (Figure 3E, F), which is consistent with the predicted molecular recognition contacts based on structure-activity relationships (SAR) reported previously (22). Besides, the ribose of NMN which is in *3′-endo* conformation forms one hydrogen bond with N7 of G41 (Figure 3E, F). Hence, the interactions between C54, G41 and NMN moiety generate a base triple, which is sandwiched by G6-U7-C40-A55 and C5-G42-A53 (Figure 3D, Supplementary Figure S5A, B, D, E). To evaluate the importance of these specific interaction in NAD$^+$ recognition, we made mutation on G41 and C54. The four mutants G41U, C54A, G41A/C54U and G41U/C54A did not show binding activity according to our ITC experiments, and thus are consistent with our observation in the structure (Figure 3G, Supplementary Figure S6).

The NAD$^+$-II riboswitch discriminates NADH (the reduced form) against NAD$^+$ (the oxidized form), and we therefore considered potential structural elements that ac-

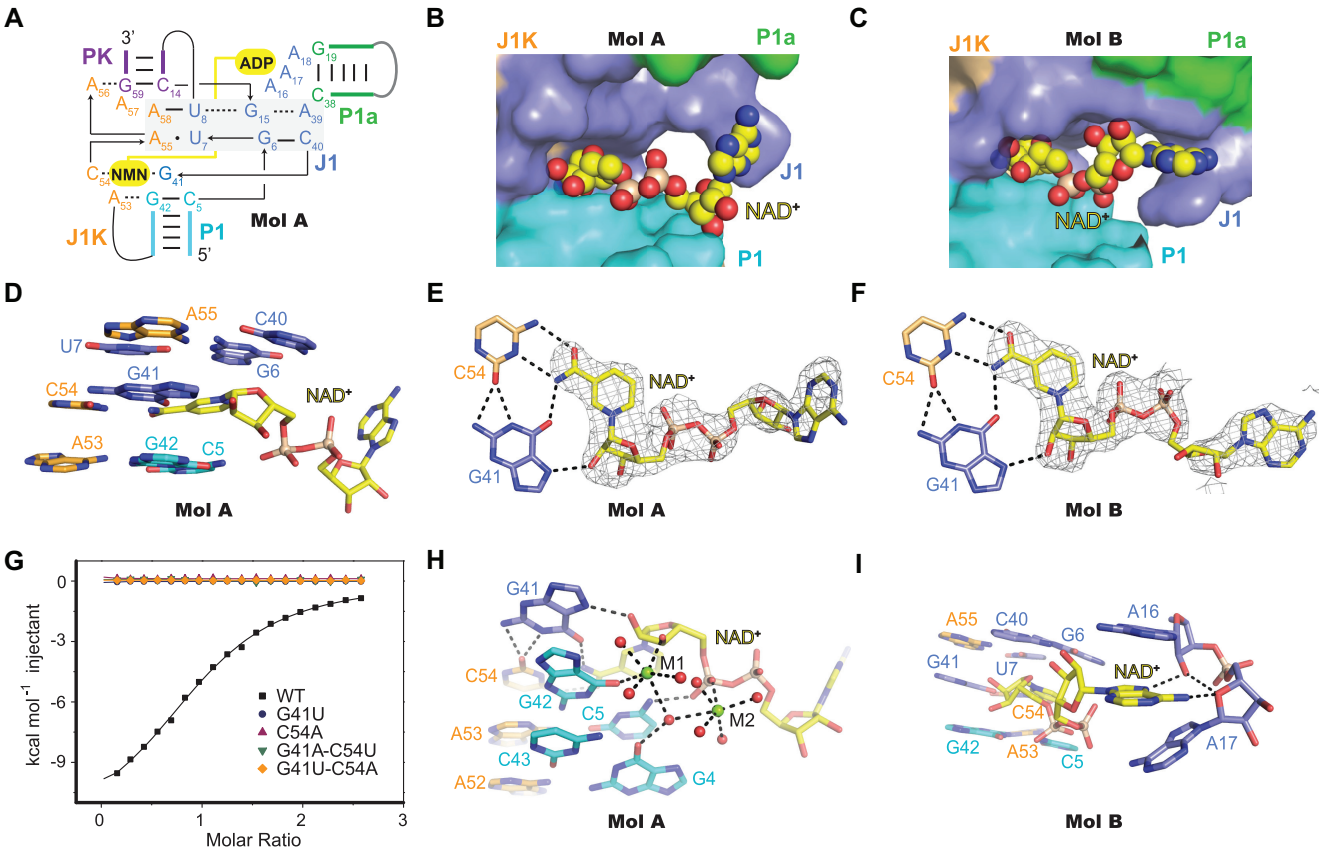

Figure 3. Structure detail of the binding pocket with NAD^+. (**A**) Schematic secondary structure of NAD^+-II riboswitch core architecture. (**B**) Surface representation of NAD^+-II riboswitch NAD^+-binding pocket in Mol A. The NMN moiety of NAD^+ intercalates into the binding pocket, while the ADP moiety of NAD^+ points outside. (**C**) Surface representation of NAD^+-II riboswitch NAD^+-binding pocket in Mol B. The NMN moiety of NAD^+ intercalates the binding pocket, while the ADP moiety of NAD^+ is stacked by junction J1. (**D**) NMN moiety of NAD^+ participates in the formation of a triple with G41 and C54, which stacks between two base platform, G6-U7-C40-A55 and C5-G42-A53. (**E, F**) NMN moiety of NAD^+ in both Mol A and Mol B forms extensive hydrogen bond interaction with C54 and G41. The composite omit maps (contoured at 1.0 σ level) of the ligand NAD^+ in Mol A and Mol B is shown in (E) and (F) respectively. (**G**) Overlay of ITC titration heat plot of NAD^+-II riboswitch WT RNA in comparison with mutants concerning nucleotides G41 and C54. (**H**) Close-up view of the coordination of two Mg^{2+} cations to RNA and ligand NAD^+ in Mol A: M1 is inner-sphere coordinated with O6 of G42 and the ribose oxygen of NMN moiety of NAD^+; M2 exhibits one inner-sphere coordination with the phosphate oxygen of NAD^+, one water-mediated interaction with O6 of G4. (**I**) Hydrogen bond interactions between ADP moiety of NAD^+ with A16 and A17 from J1 in Mol B.

count for the high NAD^+ selectivity. Several oxygen atoms (indicated with red dotted balls in Supplementary Figure S7A, B), including the two non-bridging phosphate oxygens of G6, O4′ of G6, and O6 of G41, reside inside the binding pocket and create an electronegative environment to support selection for the positively charged nicotinamide ring of NAD^+ (Figure 1A, Supplementary Figure S7A, B). Besides, the nicotinamide moiety of NAD^+ is stacked on either sides to the two base pairs G42-C5 and G6-C40, respectively, with distances of 3.6 Å and 3.5 Å (Supplementary Figure S7C). This arrangement is consistent with a putative cation-π interaction that supports the discrimination of NADH against NAD^+. Additionally, the tight sandwich pocket likely favours intercalation of the planar NAD^+ pyridinium ring rather than the sterically more demanding, puckered 1,4-dihydronicotinamide ring of NADH.

The ADP moiety of NAD^+ in both Mol A and Mol B points outward from the NMN binding cavity, but adopts different conformations. In Mol A, the adenosine moiety of NAD^+ is arranged perpendicular to the plane of NMN and points to the base of A16 in junction J1 without forming any obvious interactions with the residues in the vicinity (Supplementary Figures S4A, S5A). In Mol B, the adenosine moiety of NAD^+ is kept within the plane of NMN and becomes sandwiched between A16 and A17 from junction J1 (Supplementary Figure S4B, S5D). The composite omit maps (contoured at 1.0 σ level) of NAD^+ within the binding pocket are shown in Figure 3E and F and Supplementary Figure S5A, D.

In close vicinity of NAD^+, three cations – likely Mg^{2+} – were identified in Mol A based on $2F_o$-F_c and F_o-F_c maps and guided by the coordination geometries (Figure 3H, Supplementary Figure S5C). M1 and M2 are located between NAD^+ and stem P1 (Figure 3H) and M3 is located next to NAD^+, G15, G6 and A16 (Supplementary Figure S5C). M1 is inner-sphere coordinated with O6 of G42 and the ribose 3′ oxygen of the NMN moiety, while three sites are coordinated with water molecules and the remaining one displays a water-mediated interaction with O6 of G4 and further to M2 (Figure 3H). M2 itself exhibits one inner-

sphere coordination with the phosphate oxygen of NAD^+, one water-mediated interaction with O6 of G4 (as M1), and coordination with four water molecules (Figure 3H). M3 displays four outer-sphere coordination with N7 of A16, N7 of G6, the phosphate oxygen between G15 and A16 and three water molecules (Supplementary Figure S5C). Finally, we mention that one hydrogen bond interaction is formed between the 4-NH2 group of C5 and the phosphate oxygen of NAD^+ (Figure 3H) and another one between 3′-OH of the ADP moiety and the phosphate between G2 and A3 (Supplementary Figure S5C).

In contrast to Mol A, no Mg^{2+} cation was observed in the NAD^+ binding pocket of Mol B. Instead, some water molecules were identified in the same position as M1 and M2 in Mol A to mediate the interactions between G4, G42, G6 and A16 with NAD^+ in Mol B (Figure 3I, Supplementary Figure S5F). C5 forms direct interactions with the phosphate of NAD^+; G41 forms two hydrogen bonds with the ribose of the NMN moiety; 4-NH2 of C40 and the phosphate of A39 form another three hydrogen bonds with the ribose of the ADP moiety (Supplementary Figure S5F). As mentioned before, the adenine of NAD^+ is sandwiched by the bases of A16 and A17 in Mol B (Figure 3I). In addition, the Hoogsteen edge of the ADP moiety forms two hydrogen bonds with the ribose O2′ of A17 and the ribose O4′ of A16 (Figure 3I).

Structure of the NAD^+-II riboswitch in complex with NMN

Previous in-line probing experiments indicated that the NAD^+-II riboswitch can bind to NMN with a 3-fold higher binding affinity than NAD^+ (22). Here, we also obtained well-diffracting crystals of the NAD^+-II riboswitch in complex with NMN under similar crystallization conditions and collected the diffraction data at a resolution of 2.5 Å. The NMN-bound riboswitch structure was solved using the molecular replacement method with the NAD^+-bound NAD^+-II riboswitch complex as the initial model.

The overall tertiary structure of the NMN-bound riboswitch adopts the same topology as the NAD^+-bound counterpart (Figures 4A, B and 2A). There are also two RNA molecules in one asymmetric unit, with two RNA molecules forming a dimer through base pairing between each C10 and G11, linking the two PK stems as a continual helix (Supplementary Figure S8A, B).

For one RNA molecule, the backbone of junction J1 folds as 'S' shape with two diversions to help the formation of PK, and the 3′ terminal tail J1K climbs upside within the minor groove of stem P1 similar to NAD^+-bound state (Supplementary Figure S8C, D). The ligand NMN is encapsulated between stem P1 and junction J1 like the NMN-moiety in the NAD^+-bound structure (Figure 4C–E). With the same constitution of the binding pocket, G6, U7, C40 and A55 form the four-base tier located upside of NMN, while a triple C5-G42•A53 located on the other side of NMN in both two RNA molecules (Figure 4C, Supplementary Figure S8E). Likewise, NMN itself contributes to form a triple with the noncanonical G41•C54 through four hydrogen bonds (Figure 4D). Additionally, the 3′ ribose oxygen of NMN forms a hydrogen bond with the phosphate of G41, and the phosphate oxygen of NMN forms another hydrogen bond with 4-NH2 of C5 (Figure 4D). The $2F_o - F_c$ and $F_o - F_c$ maps (contoured at 1.0 σ level) for NMN in binding pocket is shown in Figure 4C.

We aligned the NAD^+- and NMN-bound riboswitch structures and the overlay confirms the consistency of the two RNA-ligand complexes (Supplementary Figure S9A). The Mol A/A' binding pockets of NAD^+- and NMN-bound states are nearly identical (Supplementary Figure S9B, D and E). Both, the nucleotides that contribute to the recognition of NMN moiety/the bound NMN and the nucleotides such as A16, A17 that stack on the ADP moiety in the NAD^+-bound structure exhibit the same positions. Even the Mg^{2+} cation in the binding pocket of the NMN-bound riboswitch is located at the same position as M1 in the NAD^+-bound riboswitch (Supplementary Figure S9B, D and E). For Mol B, the nucleotides that contribute to the recognition of the NMN moiety and the bound NMN fragment match well. However, due the lack of the ADP moiety in the NMN-bound structure, A16 and A17 that stack on ADP moiety in NAD^+-bound structure show a different arrangement in the NMN-bound structure (Supplementary Figure S9C, F and G). We are not sure whether the different position of stem P1a and the different conformation adopted by the nucleotides of the linking segment (G15 to A18) in the two asymmetric molecules are caused by the crystal packing interactions or not. From the comparison of the two asymmetric molecules in NAD^+- and NMN-bound structures, we conclude that stem P1a is the more flexible part of the NAD^+-II riboswitch, while the helical scaffold (P1-J1/J1K-PK) that recognizes the NMN moiety is rather rigid.

Calorimetric analysis of metal ion dependent ligand binding

Previous PAGE analysis of in-line probing reactions indicated that the NAD^+-II riboswitch binds to NMN with about 3-fold higher affinity than NAD^+ (22). Therefore, we decided to also rely on NMN for the calorimetric determination of binding affinities of the NAD^+-II riboswitch and selected mutants. For the wild-type construct (*pnuC*-GA) and NMN we obtained a dissociation constant K_d of 41.1 ± 1.1 μM with an approached 1:1 stoichiometry in three replicates (Supplementary Figure S2).

For both NAD^+- and NMN-bound structures of the NAD^+-II RNA, we observed cations in the binding pocket of Mol A and Mol A', respectively. In order to examine the impact of divalent metal ions on NMN binding capacity, we prepared riboswitch samples with varying Mg^{2+} concentration, ranging from 0 mM to 20 mM, and performed isothermal titration calorimetry. Clearly, concentrations of Mg^{2+} lower than 1 mM were insufficient for ligand binding. With increasing Mg^{2+} concentration up to 20 mM, the binding affinity between riboswitch and NMN became higher (5 mM Mg^{2+}, K_d of 247 μM; 10 mM Mg^{2+}, K_d of 76 μM; 20 mM Mg^{2+}, K_d of 41 μM) (Supplementary Figure S10). We also tested the impact of other divalent cations and performed isothermal titration calorimetry in the presence of 20 mM Ca^{2+} or 20 mM Ba^{2+} instead of Mg^{2+}, under otherwise same conditions. As shown in Supplementary Figure S11, Ca^{2+} maintains binding capacity to NMN (20 mM Ca^{2+}, K_d of 58 μM), however, the sole presence of Ba^{2+}

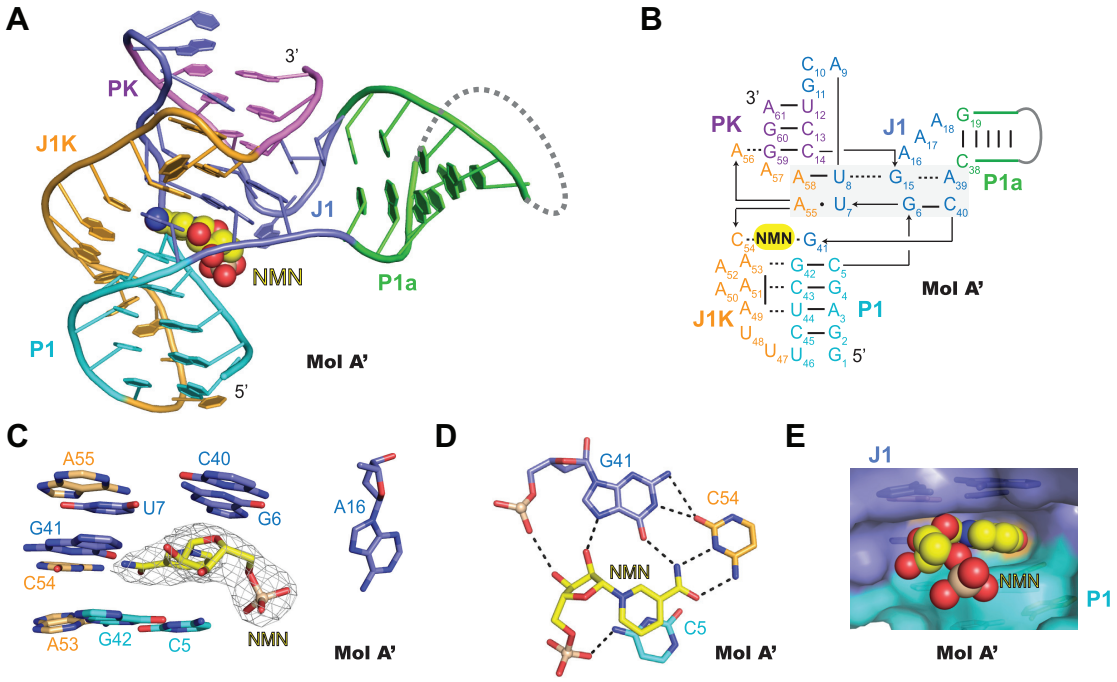

Figure 4. Structure of the NAD$^+$-II riboswitch bound to NMN. (**A**) Cartoon representation of the tertiary structure of NAD$^+$-II riboswitch in complex with NMN. Same colour code as in Figure 1 is used. (**B**) Schematic representation of the tertiary structure of NAD$^+$-II riboswitch in complex with NMN. (**C**) Architecture of the NMN-bound binding pocket in Mol A. A triple formed by NMN and nucleotides G41 and C54 stacks between two base platform, G6-U7-C40-A55 and C5-G42-A53. (**D**) Close-up view of the interactions between NMN and G41, C54, C5. (**E**) Surface representation of NAD$^+$-II riboswitch NMN-bound binding pocket.

greatly reduced the affinity to NMN (20 mM Ba^{2+}, K_d of 400 μM). These results highlight that the proper divalent metal ions must be available to support ligand binding. At this point, we note that most likely the role of Mg^{2+} for the NAD$^+$-II riboswitch is multiple and concerns stabilization of the overall RNA fold, pre-organization of the binding cavity, and a significant contribution to ligand binding that originates from bridging the ligand's phosphate and the RNA (see M1 in Figure 3H, and Supplementary Figure S9D and E).

Furthermore, we examined the impact of monovalent ions on NMN binding. We prepared RNA samples with varying K^+ concentration ranging from 0 mM to 1000 mM in the presence of 1 mM or 10 mM Mg^{2+} and performed isothermal titration calorimetry. In the presence of 1 mM Mg^{2+}, increasing K^+ concentration did not initiate binding of NMN, even when the concentration of K^+ was increased to 1000 mM. Under 10 mM Mg^{2+}, increasing K^+ concentration up to 500 mM resulted in reduced affinity to NMN (no K^+: K_d of 31 μM; 100 mM K^+: K_d of 76 μM; 500 mM K^+: K_d of 151 μM) (Supplementary Figure S12). These results indicate that the presence of monovalent ions alone is not sufficient to enable NMN binding. All thermodynamic parameters extracted from our binding experiments are listed in Supplementary Table S2.

Ligand-induced folding of the NAD$^+$-II RNA and mutation analysis

To evaluate binding thermodynamics and kinetics, we developed a 2-aminopurine (Ap) based fluorescence assay for the NAD$^+$-II riboswitch (12,27). Based on the crystal structures of the ligand-bound NAD$^+$-II riboswitch, we selected nucleoside position A57 for the single Ap substitution (Figure 5A). A57 is close to the binding pocket and directed outwards (Figure 5A). Therefore, it is expected that ligand binding can be monitored in real time by a fluorescence increase originating from the nucleobase that becomes unstacked during the ligand-induced folding process. Distinct to the construct used for crystallization, we synthesized a NAD$^+$-II construct with a 5 bp stem P1a that was closed by a GAAA tetra-loop (instead of the U1A recognition loop) and containing the A57Ap modification (Supplementary Figure S1B, Supplementary Table S3). The qualitative fluorescence response of the A57Ap riboswitch variant (0.5 μM) upon addition of Mg^{2+} (20 mM), and subsequently, of the ligands NAD$^+$ (300 μM), NMN (300 μM), and ADP (300 μM), respectively, are depicted in Figure 5B. Mg^{2+} addition alone did result in a pronounced fluorescence decrease, indicating fold compaction of the specific region around A57Ap. Addition of NAD$^+$ in 300-fold excess over RNA caused a pronounced fluorescence increase consistent with the conformational change of the reporter into an unstacked position. For the NMN (in 300-fold excess), the fluorescence increase was even more pronounced and binding was trackable in real time by the corresponding fluorescence signal, providing the kinetics of the ligand-induced folding/binding process with an observed rate k_{obs} of 0.39 ± 0.04 s^{-1} (Figure 5C). In contrast to NMN, addition of ADP did not result in an altered fluorescence signal. This is consistent with our structure analysis that revealed that the ADP moiety of NAD is not specifically recognized

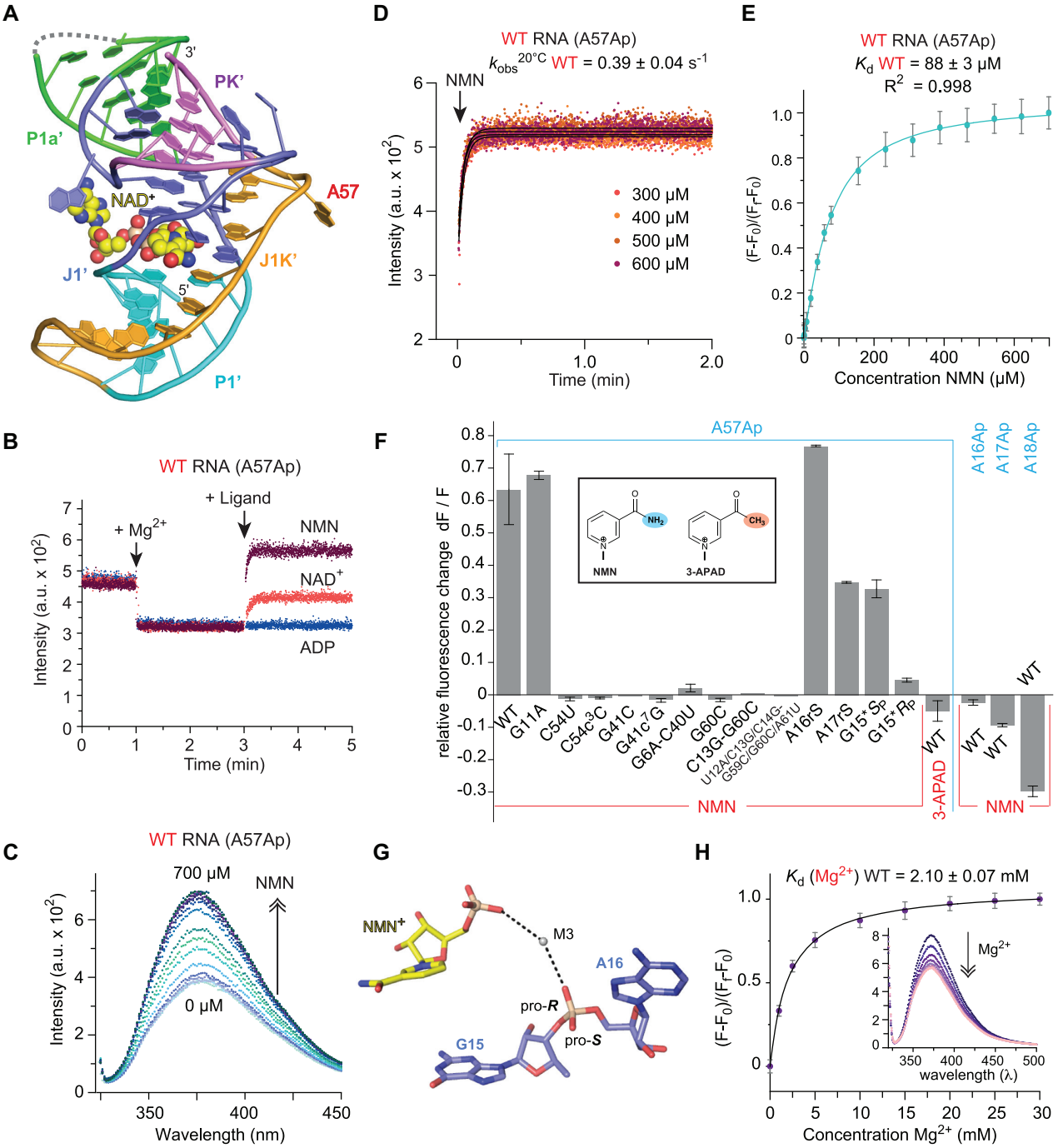

Figure 5. Fluorescence spectroscopic assessment of the NAD$^+$-II riboswitch. (**A**) Cartoon representation of the tertiary structure of NAD$^+$-II riboswitch bound with NAD$^+$, in which A57 is close to the binding pocket and directed outwards. (**B**) Qualitative fluorescence response of the A57Ap riboswitch variant (0.5 µM) upon addition of Mg^{2+} (20 mM), and subsequently, of the ligands NAD$^+$ (300 µM), NMN (300 µM), or ADP (300 µM). (**C–E**) Fluorescence change upon titration of A57Ap with increasing concentration of NMN (in 300-fold excess), which provide the kinetics of the ligand-induced folding/binding process with an observed rate k_{obs} of 0.39 ± 0.04 s^{-1}. (**F**) Mutational analysis was performed by the A57Ap fluorescence assay to verify specific interactions seen in the crystal structures. Chemical structures of NMN and 3APAD nucleobases are shown. (**G**) Metal ion M3 is localized between the RNA backbone (G15-G16) and ligand phosphate in one molecule of the asymmetric unit, in both NAD$^+$ and NMN bound structures. (**H**) Ap fluorescence assay to determination the affinity of Mg^{2+} for the NAD$^+$-II riboswitch in the absence of NMN ligand. 3APAD (3-acetylpyridine-adenine dinucleotide).

by the NAD$^+$-II pocket (Figure 3B, C). We determined the affinity of NMN to wild-type NAD$^+$-II RNA with this fluorescence spectroscopic approach (as an alternative to ITC), and as expected obtained a K_d value in the lower μM region (Figure 5D, E).

Our main application for the A57Ap fluorescence assay was mutational analysis to verify specific interactions seen in the crystal structure (Figure 5F, Supplementary Figure S13). First, we tested the disruption of dimers by replacing G11 with A in the dimerization site (C10-G11). We observed the same strong fluorescence response as observed for the wildtype RNA which confirms full functionality of NAD$^+$-II monomers. Next, we analysed the recognition of the NMN amide group by the Watson-Crick face of C54. Both, C54U and 3-deazacytidine (C54c^{3}C) mutants gave no response upon NMN addition (Figure 5F). Also, G41 that recognizes the sugar edge of NMN cannot be replaced without loss of binding affinity (G41C, G41c^{7}G) (Figures 5F, 3E, F). The base tetrad G6-U7-C40-A55 forms the ceiling of the binding pocket above the ligand (Figure 2G, 3D). Thereby, the G6-C40 Watson-Crick pair interacts via its minor groove with U7 and A55. Altering the minor groove donor acceptor pattern through replacement with A6-U40 abolished binding capability (Figure 5F). Next, we evaluated the pseudoknot whose 3-bp sequence is absolutely conserved (Supplementary Figure S1A). Any mutation we tested, such as a single G60C, the compensatory base pair mutation C13G-G60C, or the full pseudoknot inversion U12A/C13G/C14G-G59C/G60C/A61U was not tolerated (Figure 5F). In contrast, mutations in the sequence junction J1 (A16, A17, A18) retained binding capability even when the complete nucleobase was removed and only a ribose spacer was present (A16rS, A17rS) (Figure 5F). Next, we evaluated the impact of a Mg^{2+} ion that was localized between the RNA backbone (G15-G16) and ligand phosphate in one of the molecules of the asymmetric unit, in both NAD$^+$ and NMN bound structures (Figure 5G, Supplementary Figure S5C). We synthesized the diastereomerically pure G15 R_P and S_P phosphorothioates of NAD$^+$-II RNAs (Supplementary Figure S14). The phosphate-ligand mediating metal ion interaction seems indeed crucial for activity because the A57Ap fluorescence response is significantly lower for G15 R_P compared to the S_P counterpart (Figure 5G). Furthermore, we note that 3-acetylpyridinadenosinediphosphate (3-APAD), a NAD$^+$ analog that lacks the amide group for recognition/base pairing to C54, did not respond in our assay (Figure 5F). Finally, we intended to test the flexible A16-A17-A18 region with individual Ap substitutions. While A16Ap and A17Ap did not provide a fluorescence change upon ligand binding, A18Ap experienced a significant fluorescence decrease (Figure 5F). A18 is exposed in Mol B of the NAD$^+$-bound riboswitch but stacked in Mol A (Supplementary Figure S4). It is therefore tempting to assume that in solution, the conformation of the junctional A16-A17-A18 nucleosides of the NAD$^+$-II riboswitch resembles the conformation we observe in Mol A.

Finally, we applied the Ap fluorescence assay to determine the affinity of Mg^{2+} for the NAD$^+$-II riboswitch in the absence of NMN ligand (Figure 5H). A dissociation constant K_d of 2.10 ± 0.07 mM was obtained for the wildtype RNA with the A57Ap sensor. This value is consistent with the findings described above that divalent metal ions are required for NMN binding of the NAD$^+$-II riboswitch.

Tailoring a minimal NMN aptamer module

The two RNA molecules in each asymmetric crystallographic unit of the ligand-bound NAD$^+$-II riboswitch display a different orientation of their stems P1a, and hence, indicate higher conformational flexibility of stem P1a with respect to the rest of the RNA fold (Figure 1E). The NMN-binding pocket is part of the core of the NAD$^+$-II fold (Figure 6A, B) involving in J1 and J1K, while stem P1a is not directly involved in ligand recognition (Figures 4, 6A, B). More precisely, G15 and A39 can be regarded as the connecting nucleotides of stem P1a to the core of the RNA fold. At the same time, these nucleotides are key determinants of the core by converging and directly participating in the formation of the base tetrad tier above the bound ligand (Figure 2F, Supplementary Figure S3C). These observations stimulated us to explore whether the aptamer scaffold can be simplified/shortened in sequence by directly joining the nucleosides G15 and A39, thereby lacking stem P1a (Figure 6A, B). Consequently, we synthesized five ΔP1a RNA constructs comprising one to four cytidines, and one construct with a direct linkage between G15 and A39 (Figure 6A). All of them were analysed for binding NMN using isothermal titration calorimetry (ITC) (Figure 6D). It turned out that except the C_4 linkage all others were well tolerated, with C_3 providing the highest affinity for NMN (K_d^{ITC} of 18.3 ± 1.2 μM) (Figure 6D, Supplementary Figure S15, Supplementary Table S2). We further determined the binding affinities of the C_1 and C_0 RNA constructs to NAD$^+$ and ADP by ITC (Figure 6E, F). These two engineered NAD$^+$-II aptamers show significantly lower binding affinity to NAD$^+$ and no binding affinity to ADP (Figure 6E, F; Supplementary Figure S16, Supplementary Table S2), retaining the selectivity characteristics of the original NAD$^+$-II riboswitch containing stem P1a.

CONCLUDING REMARKS

To date, two classes of NAD$^+$ sensitive riboswitches are known (18,22). The *nadA* RNA motif was reported first and is now referred to as NAD$^+$-I riboswitch; it contains two tandem domains with similar architecture. In contrast, the *pnuC* RNA motif (NAD$^+$-II riboswitch) contains only one domain (18,22) (Supplementary Figure S1A). The present structures of NAD$^+$-II RNA bound with NAD$^+$ or NMN reveal a unique RNA fold with multiple tiers of base tetrads and base triples assembled from the large internal loop and nucleosides from the 3′-tail (Figure 2-4). The 3′-tail folds back on helix P1 and the central base tiers, and finally promotes the formation of the coaxially stacked 3 bp pseudoknot double helix (Figure 2A). The pseudoknot harbours the Shine-Dalgarno (SD) sequence, which creates the molecular basis for switching off the translation of the downstream coding region of the mRNA by sequestration. Initial biochemical studies on the class-II NAD$^+$ riboswitch suggested that the NAD$^+$-II aptamer specifically recognizes the NMN moiety of NAD$^+$ (22). The crystallographic stud-

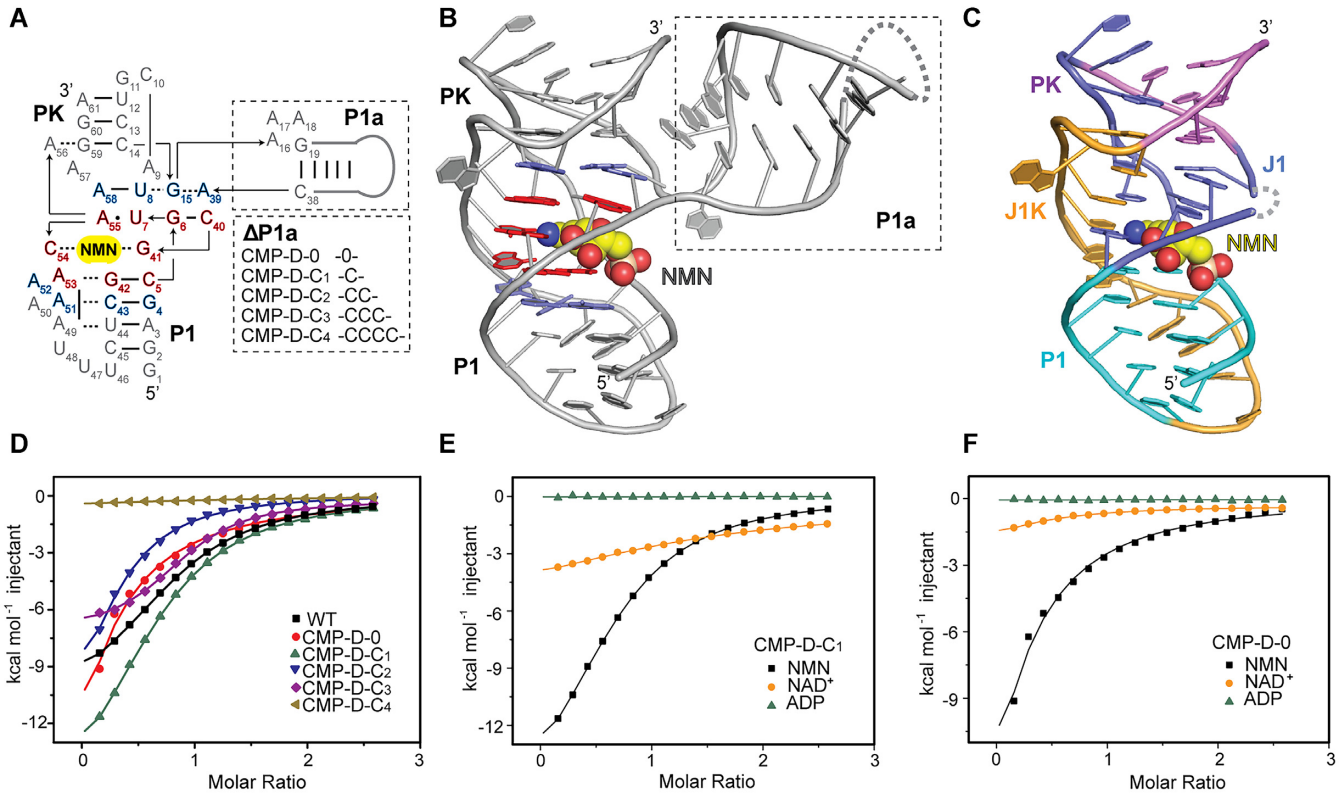

Figure 6. Minimizing of the NAD$^+$-II riboswitch fold. (**A**) Schematic representation of the tertiary structure of NAD$^+$-II riboswitch in complex with NMN, in which the residues that constitute the ligand binding pocket were shown in red and blue. Stem P1a and the variant sequences used to substitute stem P1a were labeled with dashed rectangles. (**B**) Cartoon representation of the tertiary structure of NAD$^+$-II riboswitch in complex with NMN. Same colour code as in Panel (A) is used. Stem P1a is shown with a dashed rectangle. (**C**) Cartoon representation of the tertiary structure of the tailored NAD$^+$-II riboswitch without stem P1a. (**D**) Overlay of ITC titration heat plot of NAD$^+$-II riboswitch WT RNA in comparison with the truncated RNA molecules containing variant sequences to replace stem P1a. (**E**) Comparison of ITC titration heat plot of the truncated NAD$^+$-II riboswitch with one C instead of the section A16-C38 binding to NMN, NAD$^+$ and ADP. (**F**) Comparison of ITC titration heat plot of the truncated NAD$^+$-II riboswitch with direct linkage between A15-C39 binding to NMN, NAD$^+$ and ADP.

ies presented here reveal the detailed molecular architecture of the recognition mode. Conserved residues that are distributed dispersively in the secondary structure among stem P1, loop segments J1 and J1K are brought into close proximity to constitute the NMN moiety binding pocket in the tertiary structure. The NMN moiety is directly recognized by G41 from the internal loop J1 and C54 from the tail J1K, which is further stacked by multiple base tiers (Figures 2, 3). Unlike the class-I NAD$^+$ riboswitch (*nadA* RNA motif) that specifically recognizes the ADP moiety of NAD$^+$, the class-II NAD$^+$ riboswitch (*pnuC* RNA motif) did not form specific interaction with the ADP moiety of NAD$^+$. Comparing the binding modes of class-I and class-II NAD$^+$ riboswitches, it remains an open question why the two classes apply complementary recognition modes sensing distinct parts of the NAD$^+$ ligand and what the precise functional reasons are for these different RNA layouts. Further thorough experimentation is needed to obtain answers that contribute to a comprehensive picture of gene regulation by mRNA NAD$^+$ riboswitches.

The structural versatility of RNA is a key prerequisite for RNA to be able to take over a plethora of functional roles in the cell (28). Structural research on gene regulating mRNA riboswitches has revealed a large number of unique tertiary RNA folds. Several examples exist that use this information to employ *in vitro* selection approaches to reprogram the natural RNA folds to host new small molecule binding sites while keeping the original overall architectures intact (29,30). For instance, the fluorescent aptamer Squash was developed from the native adenine riboswitch (31). Thereby, the evolutionary conserved peripheral scaffold of this riboswitch with its characteristic tertiary structure was kept, while the nucleotides forming the ligand binding pocket were randomized to create RNA libraries for *in vitro* systematic evolution of ligands by exponential enrichment (SELEX). Subsequent structural investigation confirmed that the native stable RNA scaffold can tolerate large local deviations from a parent structure to accommodate new ligands (32). Complementary to the *in vitro* selection approach, our investigation on the recently identified *pnuC* RNA motif demonstrates that simple structure-based rational minimization of the overall RNA scaffold is also possible. In this case, the ligand selectivity characteristics of the wild-type riboswitch are retained. Effective RNA fold minimization according to the guidelines outlined above has also been demonstrated for the preQ$_1$-II riboswitch previously (33). Such simple and effective RNA structure minimizations in combination with *in vitro* selec-

tion approaches to adjust for the desired ligand target might be useful in the course of the redesign of larger and more complex riboswitch systems (34,35).

DATA AVAILABILITY

Atomic coordinates and structure factors for the reported crystal structures of *punC* RNA motif in complex with NAD^+ and NMN have been deposited with the Protein Data bank (www.rcsb.org) under accession numbers 8GXB and 8GXC respectively.

SUPPLEMENTARY DATA

Supplementary Data are available at NAR Online.

ACKNOWLEDGEMENTS

We thank the staff members of the Large-scale Protein Preparation System, BL-17B, BL18U1 and BL-19U1 beamlines at the National Facility for Protein Science in Shanghai (NFPS), Zhangjiang Lab, China for providing technical support and assistance in data collection and analysis. We thank the staff of the BL-17U1 beamline at the National Center for Protein Sciences Shanghai (NCPSS) at SSRF for their assistance in X-ray data collection. We thank the technical assistance from the core facility of the Life Sciences Institute (LSI), Zhejiang University.

FUNDING

National Natural Science Foundation of China [32022039, 31870810, 91940302, 91640104 to A.R.]; National Key Research and Development Project of China [2021YFC2300300]; outstanding youth fund of Zhejiang Province [LR19C050003 to A.R.]; Fundamental Research Funds for the Central Universities [2017QN81010 to A.R.]; new faculty start-up funds from Zhejiang University (to A.R.); Austrian Science Fund FWF [P31691, F8011-B to R.M.]; Austrian Research Promotion Agency FFG [West Austrian BioNMR 858017 to R.M.]. Funding for open access charge: National Natural Science Foundation.
Conflict of interest statement. None declared.

REFERENCES

1. Nahvi,A., Sudarsan,N., Ebert,M.S., Zou,X., Brown,K.L. and Breaker,R.R. (2002) Genetic control by a metabolite binding mRNA. *Chem. Biol.*, **9**, 1043.
2. Winkler,W., Nahvi,A. and Breaker,R.R. (2002) Thiamine derivatives bind messenger rnas directly to regulate bacterial gene expression. *Nature*, **419**, 952–956.
3. Winkler,W.C., Cohen-Chalamish,S. and Breaker,R.R. (2002) An mRNA structure that controls gene expression by binding FMN. *Proc. Nat. Acad. Sci. U.S.A.*, **99**, 15908–15913.
4. Mironov,A.S., Gusarov,I., Rafikov,R., Lopez,L.E., Shatalin,K., Kreneva,R.A., Perumov,D.A. and Nudler,E. (2002) Sensing small molecules by nascent RNA: a mechanism to control transcription in bacteria. *Cell*, **111**, 747–756.
5. Breaker,R.R. (2012) Riboswitches and the RNA world. *Cold Spring Harb. Perspect. Biol.*, **4**, a003566.
6. Jones,C.P. and Ferre-D'Amare,A.R. (2017) Long-Range interactions in Riboswitch control of gene expression. *Annu. Rev. Biophys.*, **46**, 455–481.
7. Serganov,A. and Nudler,E. (2013) A decade of riboswitches. *Cell*, **152**, 17–24.
8. Garst,A.D., Edwards,A.L. and Batey,R.T. (2011) Riboswitches: structures and mechanisms. *Cold Spring Harb. Perspect. Biol.*, **3**, a003533.
9. Micura,R. and Höbartner,C. (2020) Fundamental studies of functional nucleic acids: aptamers, riboswitches, ribozymes and dnazymes. *Chem. Soc. Rev.*, **49**, 7331–7353.
10. Bedard,A.V., Hien,E.D.M. and Lafontaine,D.A. (2020) Riboswitch regulation mechanisms: RNA, metabolites and regulatory proteins. *Biochim. Biophys. Acta Gene. Regul. Mech.*, **1863**, 194501.
11. Furtig,B., Nozinovic,S., Reining,A. and Schwalbe,H. (2015) Multiple conformational states of riboswitches fine-tune gene regulation. *Curr. Opin. Struct. Biol.*, **30**, 112–124.
12. Haller,A., Souliere,M.F. and Micura,R. (2011) The dynamic nature of RNA as key to understanding riboswitch mechanisms. *Acc. Chem. Res.*, **44**, 1339–1348.
13. Scull,C.E., Dandpat,S.S., Romero,R.A. and Walter,N.G. (2021) Transcriptional riboswitches integrate timescales for bacterial gene expression control. *Front. Mol. Biosci.*, **7**, 1–10.
14. Brewer,K.I., Greenlee,E.B., Higgs,G., Yu,D., Mirihana Arachchilage,G., Chen,X., King,N., White,N. and Breaker,R.R. (2021) Comprehensive discovery of novel structured noncoding rnas in 26 bacterial genomes. *RNA Biol.*, **18**, 2417–2432.
15. McCown,P.J., Corbino,K.A., Stav,S., Sherlock,M.E. and Breaker,R.R. (2017) Riboswitch diversity and distribution. *RNA*, **23**, 995–1011.
16. Breaker,R. (2022) The biochemical landscape of riboswitch ligands. *Biochemistry*, **61**, 137–149.
17. Cochrane,J.C. and Strobel,S.A. (2008) Riboswitch effectors as protein enzyme cofactors. *RNA*, **14**, 993–1002.
18. Malkowski,S.N., Spencer,T.C.J. and Breaker,R.R. (2019) Evidence that the nadA motif is a bacterial riboswitch for the ubiquitous enzyme cofactor NAD(.). *RNA*, **25**, 1616–1627.
19. Weinberg,Z., Lunse,C.E., Corbino,K.A., Ames,T.D., Nelson,J.W., Roth,A., Perkins,K.R., Sherlock,M.E. and Breaker,R.R. (2017) Detection of 224 candidate structured rnas by comparative analysis of specific subsets of intergenic regions. *Nucleic Acids Res.*, **45**, 10811–10823.
20. Chen,H., Egger,M., Xu,X., Flemmich,L., Krasheninina,O., Sun,A., Micura,R. and Ren,A. (2020) Structural distinctions between NAD+ riboswitch domains 1 and 2 determine differential folding and ligand binding. *Nucleic Acids Res.*, **48**, 12394–12406.
21. Huang,L., Wang,J. and Lilley,D.M.J. (2020) Structure and ligand binding of the ADP-binding domain of the NAD+ riboswitch. *RNA*, **26**, 878–887.
22. Panchapakesan,S.S.S., Corey,L., Malkowski,S.N., Higgs,G. and Breaker,R.R. (2021) A second riboswitch class for the enzyme cofactor NAD. *RNA*, **27**, 99–105.
23. Pikovskaya,O., Serganov,A.A., Polonskaia,A., Serganov,A. and Patel,D.J. (2009) Preparation and crystallization of riboswitch-ligand complexes. *Methods Mol. Biol.*, **540**, 115–128.
24. Adams,P.D., Afonine,P.V., Bunkoczi,G., Chen,V.B., Davis,I.W., Echols,N., Headd,J.J., Hung,L.W., Kapral,G.J., Grosse-Kunstleve,R.W. *et al.* (2010) PHENIX: a comprehensive Python-based system for macromolecular structure solution. *Acta. Crystallogr. D Biol. Crystallogr.*, **66**, 213–221.
25. Emsley,P. and Cowtan,K. (2004) Coot: model-building tools for molecular graphics. *Acta. Crystallogr. D Biol. Crystallogr.*, **60**, 2126–2132.
26. Murshudov,G.N., Vagin,A.A. and Dodson,E.J. (1997) Refinement of macromolecular structures by the maximum-likelihood method. *Acta. Crystallogr. D Biol. Crystallogr.*, **53**, 240–255.
27. Souliere,M.F., Haller,A., Rieder,R. and Micura,R. (2011) A powerful approach for the selection of 2-aminopurine substitution sites to investigate RNA folding. *J. Am. Chem. Soc.*, **133**, 16161–16167.
28. Xu,B., Zhu,Y., Cao,C., Chen,H., Jin,Q., Li,G., Ma,J., Yang,S.L., Zhao,J., Zhu,J. *et al.* (2022) Recent advances in RNA structurome. *Sci. China Life Sci*, **65**, 1285–1324.
29. Porter,E.B., Polaski,J.T., Morck,M.M. and Batey,R.T. (2017) Recurrent RNA motifs as scaffolds for genetically encodable small-molecule biosensors. *Nat. Chem. Biol.*, **13**, 295–301.

30. Ishida,S., Terasaka,N., Katoh,T. and Suga,H. (2020) An aminoacylation ribozyme evolved from a natural tRNA-sensing T-box riboswitch. *Nat. Chem. Biol.*, **16**, 702–709.
31. Dey,S.K., Filonov,G.S., Olarerin-George,A.O., Jackson,B.T., Finley,L.W.S. and Jaffrey,S.R. (2021) Repurposing an adenine riboswitch into a fluorogenic imaging and sensing tag. *Nat. Chem. Biol.*, **18**, 180–190.
32. Truong,L., Kooshapur,H., Dey,S.K., Li,X., Tjandra,N., Jaffrey,S.R. and Ferré-D'Amaré,A.R. (2022) The fluorescent aptamer Squash extensively repurposes the adenine riboswitch fold. *Nat. Chem. Biol.*, **18**, 191–198.
33. Soulière,M.F., Altman,R.B., Schwarz,V., Haller,A., Blanchard,S.C. and Micura,R. (2013) Tuning a riboswitch response through structural extension of a pseudoknot. *Proc. Natl. Acad. Sci. U.S.A.*, **110**, 3256–3264.
34. Su,Y. and Hammond,M.C. (2020) RNA-based fluorescent biosensors for live cell imaging of small molecules and rnas. *Curr. Opin. Biotechnol.*, **63**, 157–166.
35. Su,Y., Hickey,S.F., Keyser,S.G.L. and Hammond,M.C. (2016) In vitro and in vivo enzyme activity screening via RNA-based fluorescent biosensors for S-adenosyl-l-homocysteine (SAH). *J. Am. Chem. Soc.*, **138**, 7040–7047.